Chapter 3

Bar Diagnostics in Edge-On Spiral Galaxies. I. The Periodic Orbits Approach

Abstract

We develop diagnostics to detect the presence and orientation of a bar in an edge-on disk, using its kinematical signature in the position-velocity diagram (PVD) of a spiral galaxy observed edge-on. Using a well-studied barred spiral galaxy mass model, we briefly review the orbital properties of two-dimensional non-axisymmetric disks and identify the main families of periodic orbits. We use those families as building blocks to model real galaxies and calculate the PVDs obtained for various realistic combinations of periodic orbit families and for a number of viewing angles with respect to the bar. We show that the global structure of the PVDs is a reliable bar diagnostic in edge-on disks. Specifically, the presence of gaps between the signatures of the periodic orbit families in the PVDs follows directly from the non-homogeneous distribution of the orbits in a barred galaxy. Similarly, material in the two so-called forbidden quadrants of the PVDs results from the elongated shape of the orbits. We show how the shape of the signatures of the dominant x_1 and x_2 families of periodic orbits can be used efficiently to determine the viewing angle with respect to the bar and, to a lesser extent, to constrain the mass distribution of an observed galaxy. We also address the limitations of the models when interpreting observational data.

3.1 Introduction

The classification of spiral galaxies along the Hubble sequence (Sandage 1961) is difficult for highly inclined systems. The tightness of the spiral arms and the degree to which they are resolved into stars and H II regions are useless criteria when dealing with edge-on galaxies. Only one main criterion remains: the relative importance of the bulge with respect to the disk. The problem is more acute when it comes to determining if a galaxy is barred, as there is no easy way to identify a bar in an edge-on system. The presence of a plateau in the light distribution of a galaxy (typically the light profile along the major axis) is often taken to indicate the presence of a bar (e.g. de Carvalho & da Costa 1987; Hamabe & Wakamatsu 1989). However, this method has two serious shortcomings: axisymmetric features might be mistaken for a bar (e.g. a lens would probably produce a very similar effect) and end-on bars are likely to be missed (their plateau would be both short and, in early type barred galaxies, superposed on the steep light profile of the bulge). The studies of the galaxy NGC 4762 by Burstein (1979a, 1979b), Tsikoudi (1980), Wakamatsu & Hamabe (1984), and Wozniak (1994) illustrate the uncertainties resulting from using such a method. It is clear that a photometric or morphological identification of bars in edge-on spiral galaxies is problematic and unsatisfactory.

Kuijken & Merrifield (1995; see also Merrifield 1996) were the first to demonstrate that a kinematical identification of bars in external edge-on spiral galaxies was possible. They calculated the projection of periodic orbits in a barred galaxy model for various lines-of-sight and showed that an edge-on barred disk produces characteristic double-peaked line-of-sight velocity distributions which would not occur in an axisymmetric disk. Equivalent methods have been used for many years in Galactic studies (e.g. Peters 1975; Mulder & Liem 1986; Binney et al. 1991; Wada et al. 1994; more recently Weiner & Sellwood 1995; Beaulieu 1996; Sevenster et al. 1997; Fux 1997a,b), since the position-velocity diagrams (PVDs) of external galaxies are analogous to the longitude-velocity diagrams of the aforementioned studies.

In this chapter, we aim to develop bar diagnostics using the PVDs of edge-on spiral galaxies in the same spirit as Kuijken & Merrifield (1995). We will, however, study the signature of each family of periodic orbits separately (before joining them to obtain a global picture) and examine how it depends on the viewing angle. We use a well-studied mass model, a well-defined method to populate the orbits, and we explore a large number of periodic orbit families. Our results should be used as a *guide* to interpret observations of the stellar and/or gaseous kinematics in edge-on spiral galaxies. While the gas streamlines can be approximated by periodic orbits, the presence of shocks will modify this behaviour significantly. Also, the collisionless stellar component is not confined to periodic or regular (quasi-periodic) orbits, and there can be a non-negligible fraction of stars on irregular orbits. Chapter 4 and Athanassoula & Bureau (1999; hereafter Paper III) will provide bar diagnostics similar to those developed here, but using, respectively, hydrodynamical and N-body simulations.

The identification of bars in edge-on spiral galaxies is not a goal in itself but rather a tool allowing us to deepen our understanding of bars. The particular line-of-sight to edge-on spirals allows us to view the kinematics of the *entire* symmetry plane of the disk in one single observation (assuming the disk is transparent) and provides a unique way of studying the dynamics of the disk globally. More importantly, such a diagnostic represents a unique opportunity to study the vertical structure of bars, of which very little is known observationally. Three-dimensional N-body simulations have shown that bars tend to buckle soon after their formation, and settle with an increased thickness and vertical velocity dispersion, appearing boxy or peanut-shaped when viewed edge-on (e.g. Combes & Sanders 1981; Combes et al. 1990; Raha et al. 1991). Beside the clues provided by the Galaxy (e.g. Blitz & Spergel 1991; Binney et al. 1991; Weiland et al. 1994), little observational data exist to directly test this hypothesis. In fact, the vertical light distribution of a bar has never been measured. Kuijken & Merrifield (1995) are the only ones to have actively searched for the kinematical signature of a large-scale bar in edge-on spiral galaxies with boxy/peanut-shaped bulges. Although their results seem to support the scenario described above, they only studied two galaxies. A similar study of a sample of thirty galaxies, most of which have a boxy or peanut-shaped bulge, will be presented in Chapter 5. The development of better bar diagnostics and the search for bars in edge-on systems are the keys to a better understanding of the vertical structure of bars. Chapters 3 and 4 of this thesis aim to fulfill the first of those needs; Chapter 5 will address the latter.

In § 3.2, we describe the mass model used in this chapter and in Chapter 4 and detail the methods adopted to calculate and populate the periodic orbits. The orbital properties of the mass model are described in § 3.3. In § 3.4, we describe the PVDs of edge-on spirals and develop kinematical bar diagnostics based on the properties of prototypical barred models with and without inner Lindblad resonances. We also generalise those diagnostics to a large range of models. The limitations of the models for interpreting spectroscopic observations are discussed in § 3.5. We summarise our results and conclude briefly in § 3.6.

3.2 Models

3.2.1 Density Distribution

The mass model used in this chapter and in Chapter 4 is the same as that used by Athanassoula (1992a,b; hereafter A92a, A92b). The results from all of those can therefore be directly compared and are complementary. We briefly review the main characteristics of the mass model here and refer the reader to A92a for a more thorough discussion of its properties.

The mass model has four free parameters which define the density distribution. The bar is represented by a Ferrers spheroid (Ferrers 1877) with density

$$\rho(x,y,z) = \begin{cases} \rho_0(1-g^2)^n & \text{for } g < 1 \\ 0 & \text{for } g \geq 1, \end{cases} \tag{3.1}$$

where $g^2 = x^2/a^2 + (y^2+z^2)/b^2$, a and b are the semi-major and semi-minor axes of the bar ($a > b$), ρ_0 is the bar central density, and (x,y,z) are the coordinates in the frame corotating with the bar. We will consider both homogeneous ($n = 0$) and inhomogeneous models; the latter with $n = 1$. The bar semi-major axis is, as in A92a, fixed at 5 kpc, but, contrary to A92a, the major axis of the bar is along the x-axis. We have thus so far introduced two free parameters: the bar axial ratio a/b (which fixes b) and the quadrupole moment of the bar Q_m (which fixes ρ_0). A92a showed how the central density, axial ratio, quadrupole moment, and mass of the bar are related. The pattern speed of the bar (Ω_p), or equivalently the distance to the Lagrange points L_1 and L_2 (r_L), constitutes a third free parameter.

The bar model described has often been used in the past and is well studied both in the context of orbital studies (e.g. Athanassoula et al. 1983; Papayannopoulos & Petrou 1983; Teuben & Sanders 1985) and of hydrodynamical simulations (e.g. Sanders & Tubbs 1980; Schwarz 1985). The main deficiency of this density distribution is that the shape and axial ratio of the bar are independent of radius.

The density distribution we use also has two axisymmetric components which, when combined together, produce a rotation curve rising relatively rapidly in the inner parts and flat in the outer parts. The first component is a Kuzmin/Toomre disk of surface density

$$\mu(r) = \frac{V_0^2}{2\pi G r_0}(1 + r^2/r_0^2)^{-3/2} \tag{3.2}$$

(Kuzmin 1956; Toomre 1963), where V_0 and r_0 are fixed to yield a maximum disk circular velocity of 164.2 km s^{-1} at 20 kpc. The second axisymmetric component is a central bulge-like spherical density distribution given by

$$\rho(R) = \rho_b(1 + R^2/R_b^2)^{-3/2}, \tag{3.3}$$

where ρ_b is the bulge central density and R_b its scalelength. The fourth free parameter of the mass model is the central concentration, $\rho_c = \rho_0 + \rho_b$ (which fixes ρ_b). The bulge scalelength is determined by imposing a fixed total mass within 10 kpc.

The models are therefore parametrised by an index n ($n = 0$ or 1) and by four free parameters: the bar axial ratio a/b, the quadrupole moment of the bar Q_m, the Lagrangian radius r_L, and the central concentration ρ_c. It should be noted that while the quadrupole moment of the bar affects all Fourier components of the potential equally, this is not the case for the bar axial ratio. The bar pattern speed and the central concentration mainly affect the existence and position of the resonances. The models considered are those of A92a (see her Table 1). We will also use her units: 10^6 $M_\odot$ for masses, kpc for lengths, and km s^{-1} for velocities. Based on a comparison with an observational sample (rotation curves, resonances positions, and Fourier components), A92a showed that these models are a fair representation of early type barred spiral galaxies.

3.2.2 Periodic Orbit Calculations

The periodic orbits allowed by a model are found using the shooting method. Through this chapter, we will only consider orbits in the plane of the disk ($z = 0$). For a given position along the y-axis ($x = 0$) and an initial velocity parallel to the x-axis ($\dot{y} = 0$), we follow a trial orbit for half a revolution in the reference frame of the bar. Other trial orbits with the same initial position but slightly different initial velocities allow iterative convergence to an orbit which "closes" after half a revolution. The orbits are integrated using a fourth-order Runge-Kutta method and the Newton-Raphson method is used to converge to the right initial velocity (Press et al. 1986). By then moving the initial position along the y-axis, it is possible to delineate a family of periodic orbits. Here, we use a constant increment along the y-axis ($\Delta y = 0.01$ kpc for all families). All periodic orbits found in this way are symmetric with respect to the minor axis of the bar. It should be noted that it is possible to have more than one periodic orbit at a given position along the y-axis (each one with a different initial velocity $\dot{x}$).

In the limit of negligible pressure, gas streamlines coincide with periodic orbits. However, contrary to periodic orbits, gas streamlines can not intersect. Thus, because we are mainly interested in studying the gaseous dynamics of barred spiral galaxies, we are not interested in periodic orbits that self-intersect or possess loops. We have therefore searched and identified only direct singly-periodic non-self-intersecting orbits, which best represent the gas flow. This constraint limits the extent of the periodic orbit families we study.

Periodic orbits can be regarded as galactic building blocks, but it is non-trivial to determine how best to use them to represent the gas distribution in a real galaxy. For stellar systems, Schwarzschild (1979) proposed a method where a linear combination (with non-negative weights) of orbits is used to reproduce the original mass distribution (yielding a self-consistent model). Here, we simply consider all the periodic orbits from certain families to be populated equally. Whenever we plot orbits, we plot an equal number of timesteps (an equal number of "points") for all orbits, independent of the period. Since we use a constant increment along the y-axis between the orbits of a given family, the resulting surface density along that axis is inversely proportional to the distance from the center (this would be true everywhere if the orbits were similar). One shortcoming of this method is that, although we have only selected individual periodic orbits which do not self-intersect and do not possess loops, orbits from a given family or from different families of periodic orbits can intersect. Such situations could not occur in the gas.

3.3 Periodic Orbit Families

As we already mentioned, periodic orbits can be thought of as the basic building blocks of the gas distribution in disk galaxies. Although they can not reproduce the properties of the gas flow in detail (e.g. the behaviour of the gas near shocks), they do give a zeroth order representation of the gas distribution and kinematics. It is thus important to understand the properties of the various periodic orbit families present in our models in order to be able to relate them to what is observed in real galaxies. A92a carried out a detailed study of the periodic orbit families located within corotation for our models. In this chapter, we will extend her study to the outer parts of the models (outside corotation) and will draw heavily on her conclusions to explain the behaviour observed in the inner parts. For a more general description of the orbital structure and the dynamics of barred spiral galaxies, we refer the reader to the excellent reviews by Contopoulos & Grosbøl (1989) and Sellwood & Wilkinson (1993).

In this section, we will describe the main properties of the basic families of periodic orbits present in the models. We will focus on two inhomogeneous bar models which are prototypes of models with and without inner Lindblad resonances (ILRs). They are, respectively: model 001 ($a/b = 2.5$, $Q_m = 4.5 \times 10^4$, $r_L = 6.0$, $\rho_c = 2.4 \times 10^4$) and model 086 ($a/b = 5.0$, $Q_m = 4.5 \times 10^4$, $r_L = 6.0$, $\rho_c = 2.4 \times 10^4$). Using the results of A92a, it is easy to extend the conclusions drawn from models 001 and 086 to most other models.

Figure 3.1 shows the characteristic diagrams of models 001 and 086. For all the periodic orbits calculated, they show the position where the orbit intersects the y-axis versus the Jacobi integral of the orbit ($E_J = E - \vec{\Omega}_p \cdot \vec{J}$). The Jacobi integral represents the energy in the rotating frame of the bar, and is the only combination of the energy and angular momentum which is conserved (neither being conserved separately in a rotating non-axisymmetric potential). All the major periodic orbit families are present. More exist, especially higher order resonance families near corotation, but they are probably unimportant for understanding the gas flow. Figure 3 of A92a shows examples of periodic orbits from the main families in model 001 (see Sellwood & Wilkinson 1993 for families outside corotation, although they use a slightly different potential). The most important families inside corotation

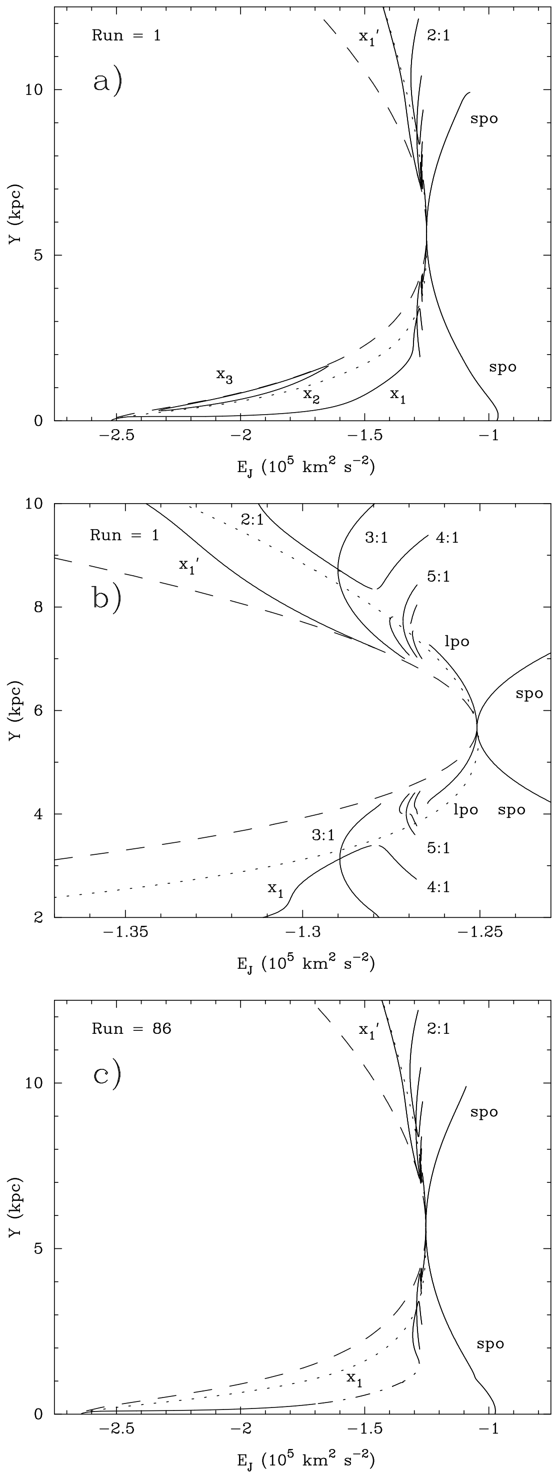

Figure 3.1: (a) Characteristic diagram of model 001. Each point represents a periodic orbit. The solid curves trace the extent of the various periodic orbit families, some of which are identified. The zero-velocity curve (ZVC) which no orbit can cross is plotted with a dashed line. The dotted line represents circular orbits in the azimuthally averaged mass distribution. (b) is simply an enlargement of (a). (c) is the same as (a) but for model 086. The section of the x_1 family plotted with a dot-dashed line represents orbits with loops.

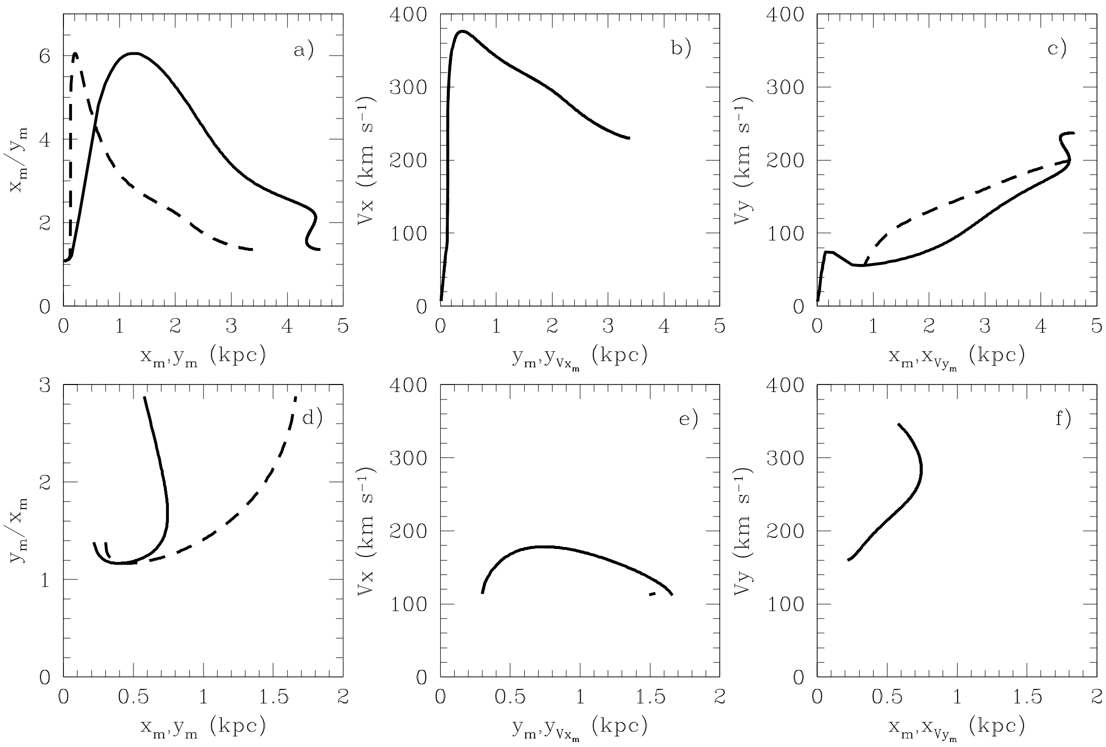

Figure 3.2: Basic properties of the x_1 and x_2 periodic orbits in model 001. (a) shows the axial ratio of the x_1 orbits as a function of their semi-major (full line) and semi-minor (dashed line) axes. (b) shows the velocity of the x_1 orbits as they cross the minor axis of the bar (full line), as well as the maximum velocity along the x-axis they reach at any point (dashed line). (c) shows the velocity of the x_1 orbits as they cross the major axis of the bar (full line), as well as the maximum velocity along the y-axis they reach at any point (dashed line). (d)–(f) are the same as (a)–(c) but for the x_2 orbits. Note that both curves are superposed in some plots.

are the x_1 and x_2. The x_1 orbits are elongated parallel to the bar and are generally thought to support it in self-consistent systems (see, e.g., Contopoulos 1980). The x_2 (and x_3) orbits are elongated perpendicular to the bar and only occur inside the ILRs. Some properties of the x_1 and x_2 periodic orbits which will be useful in the next sections are summarised in Figure 3.2. We do not consider the retrograde x_4 family here. The inner 4:1 family (four radial oscillations during one revolution) may be important for the structure of rectangular bars. Outside corotation, the dominant periodic orbit families are the x_1' and outer 2:1, corresponding to the "x_i" families inside corotation. The x_1' orbits are elongated parallel to the bar and located outside the outer Lindblad resonance (OLR). The outer 2:1 orbits are elongated perpendicular the bar and located between corotation and the OLR. The short period orbits (SPO) and long period orbits (LPO) are located around the (stable) Lagrange points L_4 and L_5 on the minor axis of the bar.

Figure 3.3 shows the main precession frequencies of models 001 and 086, obtained by azimuthally averaging the mass distribution. The major resonances are easily identified: ILRs ($\Omega_p = \Omega - \kappa/2$), inner ultra-harmonic resonance (IUHR; $\Omega_p = \Omega - \kappa/4$), corotation ($\Omega_p = \Omega$), and OLR ($\Omega_p = \Omega + \kappa/2$). Although the behaviour of the 2:1 periodic orbit families agrees with linear perturbation theory predictions outside corotation, this is not case inside corotation. In particular, despite the presence of ILRs in model 086, no x_2 orbit exists. The presence of ILRs is not enough to guarantee the existence of the x_2 family. Contopoulos & Papayannopoulos (1980) showed that the x_2 family disappears for strong bars. For this mass model, A92a showed that the x_2 orbits are absent for large bar axial ratios a/b, large bar quadrupole moments Q_m, small Lagrangian radii r_L, and for low central concentrations ρ_c (see Figs. 6 and 7 of A92a). It is thus necessary to extend the classical definition of an ILR to the strong bar case. van Albada & Sanders (1982) and A92a proposed that the existence of ILRs could be tied with the existence of the x_2 periodic orbit family and the position of the ILRs assimilated with the minimum and maximum of the x_2 characteristic curve in the characteristic diagram (of course, there might be only one ILR). We will use this definition of the existence and position of ILRs in this chapter, which explains why, despite having two ILRs in the classical sense, model 086 is considered a "no-ILRs" model. Similarly, we will assimilate the position of the IUHR with the maximum of the x_1 characteristic curve before the 4:1 gap in the characteristic diagram (A92a).

3.4 Bar Diagnostics

3.4.1 Detecting Edge-On Bars

Because of the inadequacies of a morphological identification of bars in edge-on spiral galaxies, we aim in this chapter to develop kinematical bar diagnostics, much in the spirit of Kuijken & Merrifield (1995) and Merrifield (1996). Our basic tool to identify bars in edge-on disk galaxies will be PVDs. We obtain those by calculating the projected density of material in our edge-on barred disk models as a function of line-of-sight velocity and projected position along the major axis (for various lines-of-sight). These can then be directly compared with long-slit spectroscopic observations of edge-on spiral galaxies (with the slit positioned along the major axis) or with other equivalent data set. The goal is to identify features in the PVDs which can be unmistakably associated with the presence of a bar. We discuss such features in the next sections.

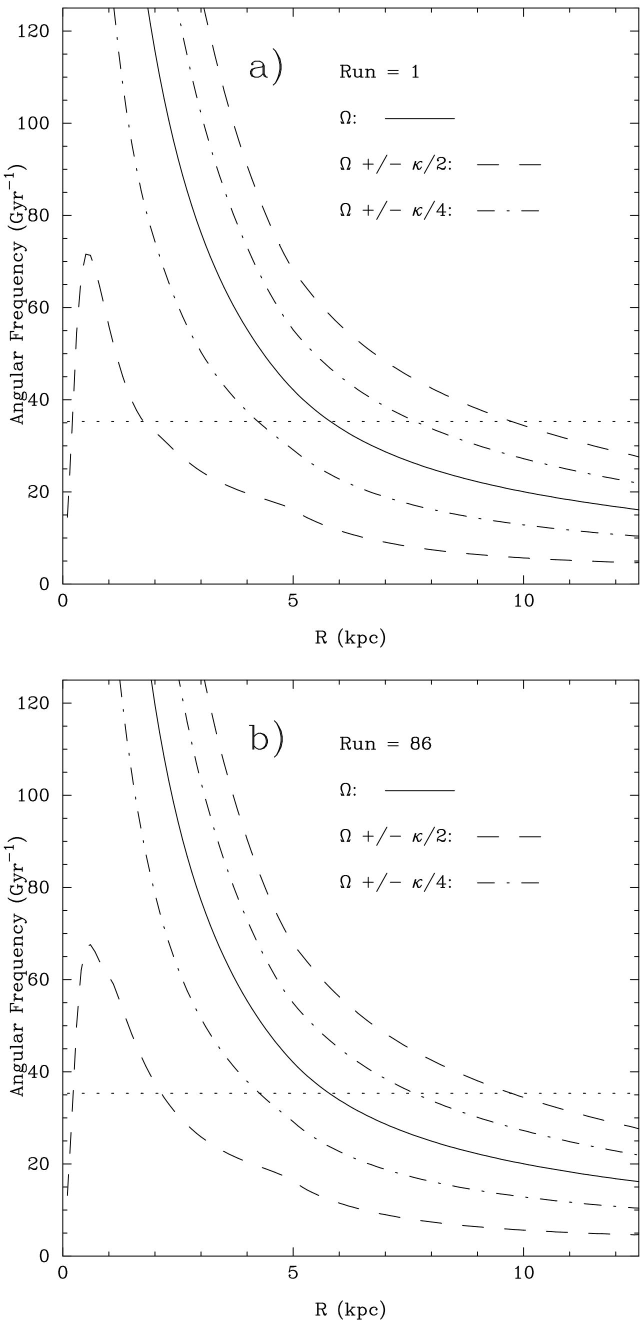

Figure 3.3: (a) Lindblad precession frequencies in the azimuthally averaged mass distribution of model 001. The various frequencies are identified on the plot. The dotted curve shows the pattern speed of the bar Ω_p in the model. (b) is the same as (a) but for model 086.

3.4.2 Model 001 (ILRs)

Figures 3.4, 3.5, and 3.6 show PVDs for, respectively, the x_1, x_2, and outer 2:1 periodic orbit families of model 001, which has ILRs (or, equivalently, has an x_2 family of periodic orbits). Each figure presents the face-on appearance of the entire family of orbits (with orbits equally spaced along the y-axis and the extent of the family limited by gaps in the characteristic curve or the appearance of loops in the orbits) and PVDs obtained using an edge-on projection and various viewing angles with respect to the bar. The viewing angle ψ is defined to be 0° when the bar is seen end-on and 90° when the bar is seen side-on.

The upper left panel of Figure 3.4 shows that, because of the high curvature of the x_1 orbits on the major axis of the bar (A92a) and the crowding of orbits at its ends, overdensities of material are created which are analogous to those caused by shocks in hydrodynamical simulations (see Sanders, Teuben, & van Albada 1983; Sanders & Tubbs 1980; A92b). As expected, very high radial velocities are present in the PVDs when the bar is seen end-on, because of streaming up and down the bar. Conversely, the velocities are low when the bar is seen side-on, as the movement is mostly perpendicular to the line-of-sight. In the next few paragraphs, we will analyse this effect in more detail, in order to understand the variation of the shape of the signature of the orbits in the PVDs as a function of the viewing angle.

In general, the trace in a PVD of a two-dimensional elongated orbit viewed edge-on can be thought of as a parallelogram. For the sake of simplicity, we will consider here an orbit which is symmetric about two perpendicular axes and which is centered at their origin, like the x_1 and x_2 orbits. If the orbit is seen exactly along one of its symmetry axes, then its trace in a PVD will be a line, both near and far sides of the orbit yielding the same radial velocity at a given projected distance from the center. In addition, the observed radial velocity will switch from positive to negative values at the center (the radial velocity is null at that point). However, for any other viewing angles, the trace of the orbit in a PVD will be strongly parallelogram-shaped, populating the "forbidden" quadrants (top-right and bottom-left quadrants of the PVDs considered here). This shape is due to the fact that, when the line-of-sight is not parallel to one of the axes of symmetry of the orbit, the near and far sides of the orbit yield different radial velocities for a given projected distance from the center, and the position at which the observed radial velocity switches from positive to negative values is not the center, but rather is displaced slightly away from it. One only needs to look at the radial component of the velocity along an elongated orbit to see that. At that position, by definition, the tangent to the orbit is perpendicular to the line-of-sight. Generally, the highest tangential velocity occurs on the minor axis of the orbit and is parallel to its major axis. The opposite is also generally true (but not

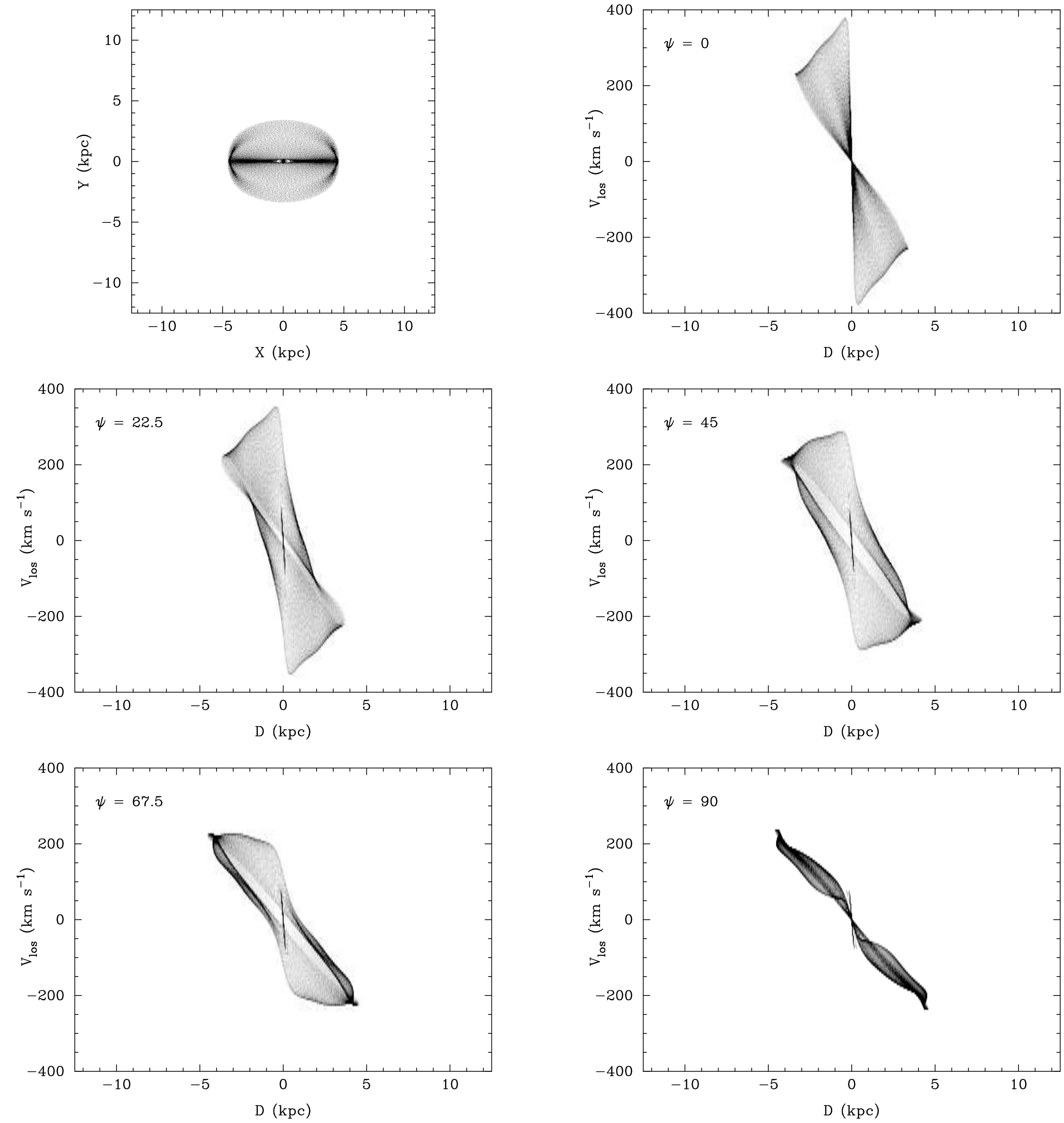

Figure 3.4: Surface density and position-velocity diagrams of the x_1 orbits in model 001. The upper-left plot shows the face-on appearance (surface density) of the orbits, as selected in the text (§ 3.2.2). The bar is horizontal, has a semi-major axis length of 5 kpc, and is rotating clockwise. The other plots show position-velocity diagrams (projected density of material as a function of line-of-sight velocity and projected position along the major axis) of the orbits when the model is viewed edge-on. The angle between the line-of-sight and the bar is indicated in the top-left corner of each diagram, a viewing angle of $\psi = 0°$ indicating that the bar is seen end-on (line-of-sight parallel to the bar) and a viewing angle of $\psi = 90°$ indicating that the bar is seen side-on (line-of-sight perpendicular to the bar).

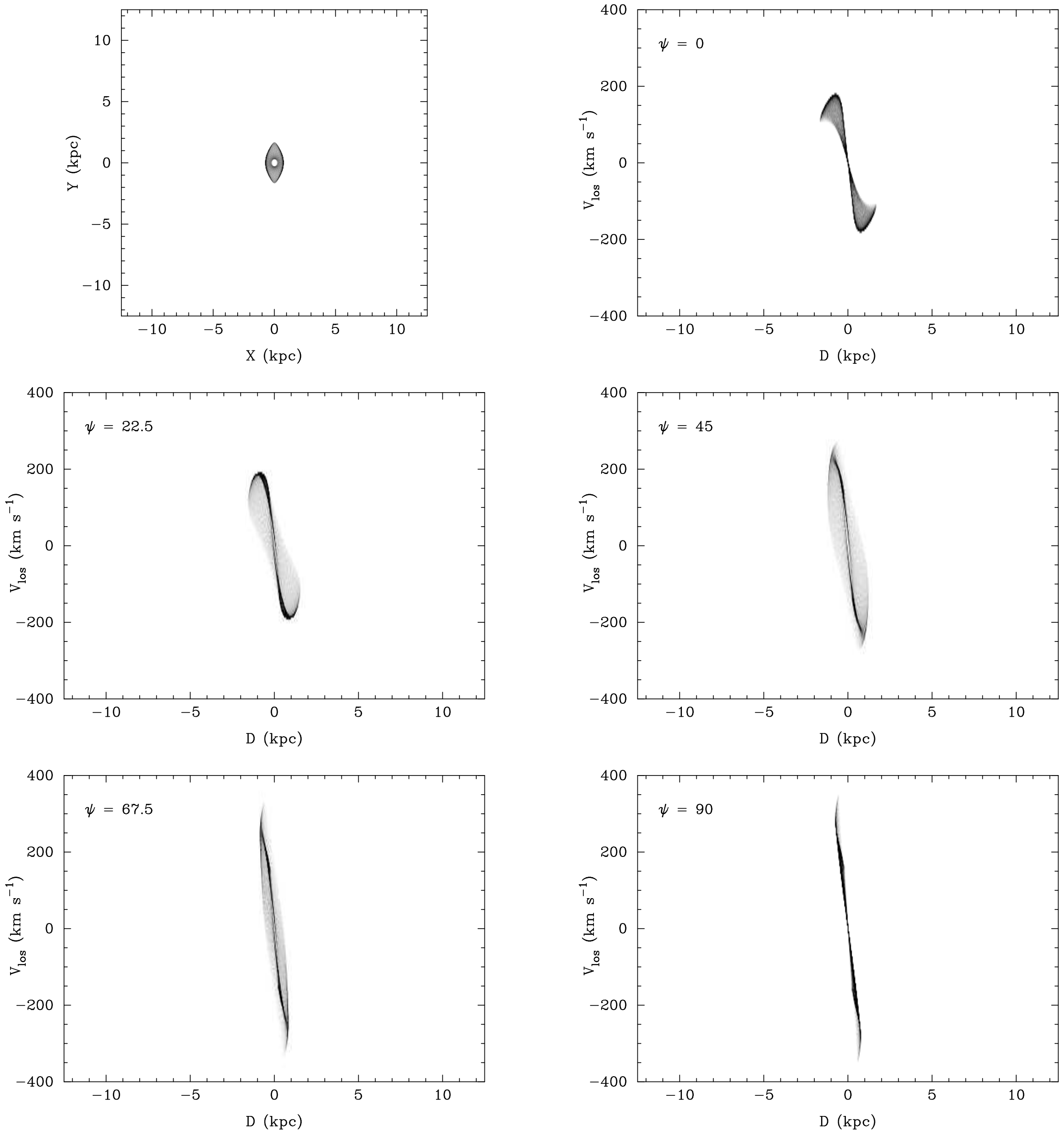

Figure 3.5: Same as Figure 3.4 but for the x_2 family of periodic orbits in model 001.

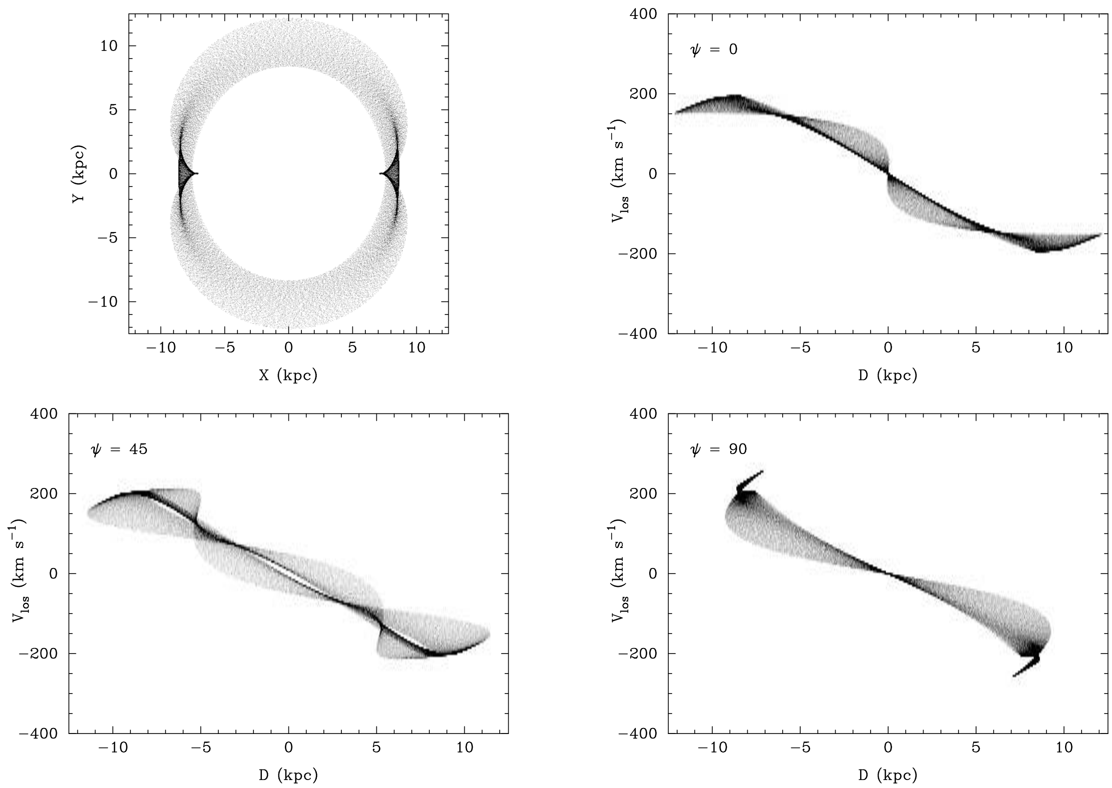

Figure 3.6: Same as Figure 3.4 but for the outer 2:1 family of periodic orbits in model 001. Note that fewer viewing angles are displayed.

always) for the lowest velocity (see, e.g., Fig. 3.2). Therefore, the parallelogram-shaped trace of an elongated orbit in a PVD is narrow but reaches high radial velocities (with respect to the local circular velocity) for viewing angles close (parallel) to its major axis, while it is rather extended and reaches only relatively low radial velocities for viewing angles close to its minor axis. The exact shape of the parallelogram in a PVD depends primarily on the axial ratio of the orbit. For a given azimuthally averaged radius, as the eccentricity of the orbit is increased, the velocity contrast of the orbit (the difference between the highest and lowest tangential velocities) also increases. The viewing angle dependence of the trace of the orbit in a PVD is thus accentuated. At the other end of the eccentricity range, the trace of a circular orbit in a PVD is an inclined straight line passing through the origin and identical for all viewing angles.

The parallelogram-shaped signature of the x_1 orbits of model 001 observed in the PVDs of Figure 3.4 can be understood based on the above principles. The axial ratio of the x_1 orbits generally increases with decreasing radius (except in the very center, see Fig. 3.2a). The inner orbits will thus reach very high radial velocities (compared to the circular velocity) at small projected distances for small viewing angles, while they will reach only low radial velocities at large viewing angles. On the other hand, the projected velocities of the outer orbits will vary little with the viewing angle because they are rounder. They will thus reach radial velocities close to the circular velocity at large projected distances for all viewing angles. Orbits of intermediate radii have intermediate axial ratios and thus intermediate behaviours in the PVDs. As one moves in in radius and in projected distance, the locus of the maxima of the traces of successive orbits in the PVDs will therefore increase rapidly for small viewing angles (see Fig. 3.2b), while it will decrease for large viewing angles (Fig. 3.2c). This is exactly the behaviour observed in the PVDs for the upper part of the envelope of the signature of the x_1 orbits (see Fig. 3.4). For orbits of very small radii, the axial ratio actually decreases rapidly with decreasing radius (the axial ratio reaches a maximum for orbits of minor axis length about 0.2 kpc; Fig. 3.2a). This explains why, for small viewing angles, the envelope of the signature of the x_1 orbits does not increase right to the center, but drops abruptly just before that. The ellipsoidal "holes" in the PVDs at intermediate viewing angles are due to the fact that we stopped the x_1 periodic orbits at the IUHR, not populating the small segments of the x_1 characteristic curve existing past the 4:1 gap in the characteristic diagram (see Fig. 2 of A92a). The holes disappear if we include orbits at larger Jacobi energy E_J (which are also rounder).

In Figure 3.5, the behaviour of the x_2 periodic orbits of model 001 can be contrasted with that of the x_1. As expected, because the x_2 orbits are elongated perpendicular to the bar (see Fig. 3 of A92a), the highest radial velocities are now reached when the bar is seen side-on, and the lowest when the bar is seen end-on. The general parallelogram shape of the PVDs is still present, but its nature is quite different from that of the signature of the x_1 orbits, shown in Figure 3.4. Contrary to the x_1 orbits, the axial ratio of the x_2 orbits generally decreases with decreasing radius (up to about 0.4 kpc, see Fig. 3.2d). The inner orbits have only a short extent and, because they are almost circular, they do not reach high radial velocities. Their projected velocity is close to the circular velocity for all viewing angles. The outer orbits, on the other hand, are highly elongated. They will thus reach only relatively low radial velocities at "large" projected distances for small viewing angles, and high velocities at "large" distances for large viewing angles (they are elongated perpendicular to the bar). The locus of the maxima of the traces of successive orbits of decreasing radius in the PVDs will therefore increase rapidly for small viewing angles (see Fig. 3.2e) and decrease for large viewing angles (Fig. 3.2f). Indeed, this behaviour is observed in the PVDs of Figure 3.5, at least for "large" projected distances. The behaviour at very small radii is dominated by the shape of the circular velocity curve, which rises rapidly with radius.

The observed behaviours of the x_1 and x_2 periodic orbits in the PVDs are qualitatively rather similar. This might be surprising on first thought, as the x_2 orbits behave very differently than the x_1 (see Fig. 3.2), but one could say that the properties of the x_2 orbits are "doubly-inverted" with respect to those of the x_1. The variations of the axial ratio of the x_1 and x_2 orbits with radius are opposite (Fig. 3.2), so the dependence of their signatures on the viewing angle with respect to their major axes will also be opposite. Furthermore, the major axes of the x_1 and x_2 orbits are perpendicular to each other. This "double inversion" leads to the similarity of the signatures in the PVDs. While this is true in a relative manner, it is not true in an absolute manner. Firstly, the envelope of the signature of the x_1 orbits reaches higher radial velocities than that of the x_2 orbits at small viewing angles, and the opposite is observed at large viewing angles. The explanation is simple: for small viewing angles, the radial velocities reached by the x_1 orbits in the *inner parts* are *increased* with respect to the circular velocity (the outer parts are unchanged), while for the x_2 orbits, the radial velocities in the *outer parts* are *decreased* with respect to the circular velocity (the inner parts are unchanged). The opposite is true at large viewing angles. Secondly, in the case of the x_1 orbits, the center of the parallelogram-shaped signature is relatively faint compared to its edges, while for the x_2 orbits, it is the center of the parallelogram which is bright, forming a strong inverted S-shape feature, and the outer parts are relatively faint. The inverted S-shape feature is not due to a single orbit leaving such a trace in the PVDs, but rather to the crowding of the traces of many successive orbits, which explains why it is so bright (an effect comparable to the spiral arms created by rotating slightly similar ellipses of increasing radii; Kalnajs 1973). Furthermore, because the axial ratio of the x_2 orbits increases with radius (outside 0.4 kpc), the trace of the largest orbit in the PVDs is not only the most extended but also is the one with the widest parallelogram shape. It therefore encompasses the traces of all the other orbits and defines largely by itself the envelope of the signature of the x_2 orbits, which is then very faint. The small "holes" present in the center of the PVDs of the x_2 periodic orbits at intermediate viewing angles are due to the fact that, although the elongation of the x_2 orbits generally decreases inward, the x_2 family does not extend up to the center (see Fig. 3.1).

Figure 3.6 illustrates the signature of the outer 2:1 orbits of model 001 in the PVDs. Because the orbits are almost circular, the upper part of the envelope reaches radial velocities close to the circular velocity at large projected distances, independent of the viewing angle. The features seen in the signature of the outer 2:1 orbits are largely due to the "dimples" in the orbits on the major axis of the bar (see Fig. 11 in Sellwood & Wilkinson 1993). As should be expected, the PVDs of the x_1' orbits (not shown) are similar to those of the outer 2:1 orbits if the viewing angles are reversed (e.g. $67.5° \rightarrow 22.5°$), the major axes of the orbits being at right angles. Both families yield a slowly-rising almost solid-body signature in the PVDs for all viewing angles.

Bars in early-type spiral galaxies and in N-body simulations tend to have a rectangular shape rather than an ellipsoidal shape (see, e.g., Sparke & Sellwood

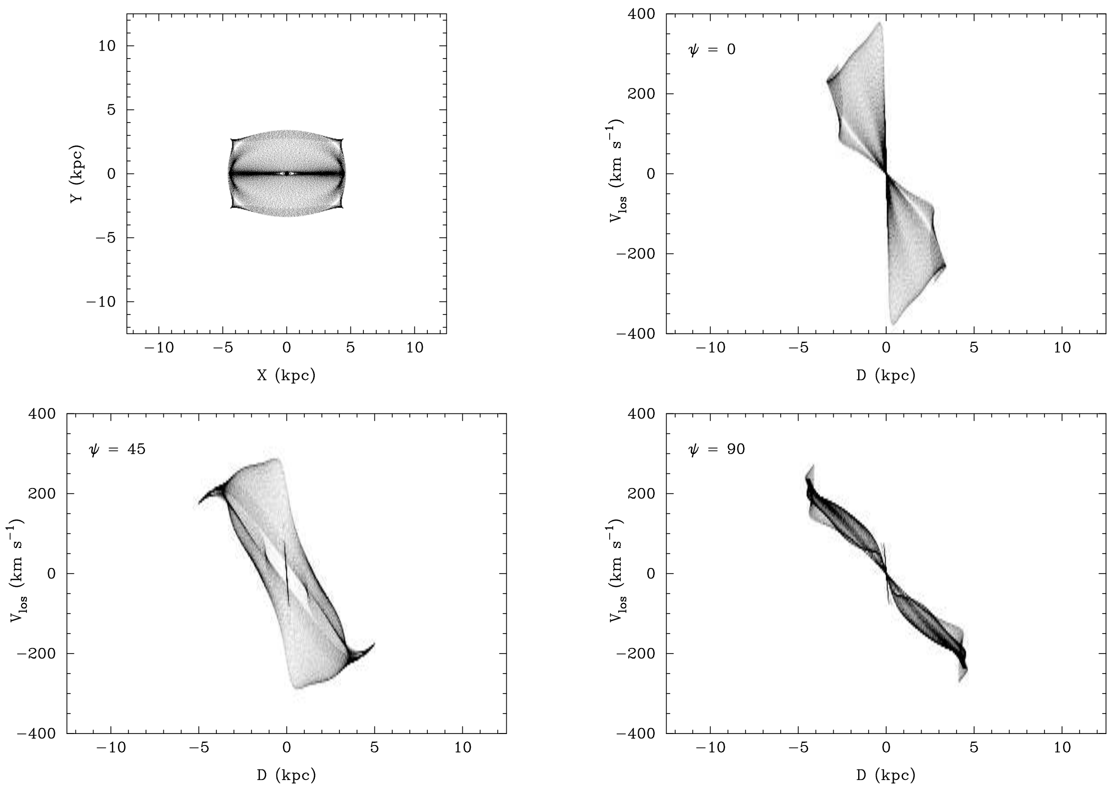

Figure 3.7: Same as Figure 3.4 but for the x_1 and inner 4:1 families of periodic orbits in model 001. Note that fewer viewing angles are displayed. Only the section of the inner 4:1 family lying outside the characteristic curve of the x_1 orbits in the characteristic diagram has been considered.

1987; Athanassoula et al. 1990). Interestingly, the maximum boxiness generally occurs just before the end of the bar (Athanassoula et al. 1990), where the x_1 orbits are slightly boxy and where the rectangular-shaped inner 4:1 orbits are found (see Fig. 3 of A92a). It is thus tempting to associate the branch of the inner 4:1 family of periodic orbits lying outside the characteristic curve of the x_1 orbits in the characteristic diagram (see Fig. 3.1) with the rectangular shape of bars. The 4:1 gap in model 001 is of type 2 (see Contopoulos 1988; A92a), so the lower branch of the 4:1 characteristic is stable and the proposed association makes sense, but this is not necessarily the case in real galaxies. In fact, early-type galaxies seem to have 4:1 gaps of type 1 (Athanassoula 1996). Figure 3.7 shows the surface density and PVDs for both the x_1 family of periodic orbits and the lower branch of the inner 4:1 family in model 001. It shows that indeed the inner 4:1 orbits can create a very rectangular surface density distribution when combined with the x_1 orbits. Although the signature of the inner 4:1 orbits in the PVDs is very peculiar and easily identifiable when taken alone, it is superposed on the signature of the x_1 orbits for most viewing angles and it is hard to disentangle the two families. However, when the bar and the inner 4:1 orbits are seen either end-on or side-on, the inner 4:1 orbits leave a signature in the PVDs distinct from that of the x_1 orbits. The lower limit of the combined envelope of the signatures of the x_1 and inner 4:1 orbits is straight and only slightly inclined at small projected distances, until it does a sharp bend at approximately the position of the IUHR (at a slightly smaller radius when $\psi = 0°$ and slightly larger radius when $\psi = 90°$, following the definition of the IUHR adopted in § 3.3). It then rises vertically until it joins with the upper limit of the envelope. This is easily understandable considering the morphology of the inner 4:1 orbits. The projected edges of the density distribution are sharpest at those viewing angles and the lines-of-sight are parallel to the approximately straight segments of the orbits (see Fig. 3.7).

The advantage of the periodic orbits approach is that various orbital components of a galaxy can be combined together in a multitude of ways. A superposition of the x_1, x_2, and outer 2:1 families of periodic orbits should give a reasonable representation of a prototypical barred galaxy with ILRs. Indeed, in the inner parts, only three direct families exist: the x_1, x_2, and x_3 (see Fig. 3.1). The x_1 orbits, parallel to the bar, are certainly present and, because the x_3 orbits are unstable (e.g. Sellwood & Wilkinson 1993), the x_2 orbits will dominate over the x_3 if orbits perpendicular to the bar are present. In the outer parts, we find the x_1' and outer 2:1 periodic orbit families. The shapes of these orbits are almost identical to those of the two subclasses of outer rings observed in barred spiral galaxies (Buta & Crocker 1991): R_1' outer rings for the outer 2:1 orbits and R_2' for the x_1' orbits. The R_1' class is dominant (Buta 1986), which explains why we considered the outer 2:1 family of periodic orbits. However, as we mentioned, the signature of the x_1' orbits in the PVDs is very similar to that of the outer 2:1 orbits (almost identical if the viewing angles are reversed) and using one or the other does not affect our conclusions or the nature of the bar diagnostics in the PVDs. Both families act as a slowly rising almost solid-body component.

Figure 3.8 shows the surface density and PVDs obtained by superposing the x_1, x_2, LPO, and outer 2:1 families of periodic orbits in model 001. The surface density of the x_1, x_2, and outer 2:1 families is qualitatively similar to what is observed for barred galaxies with an outer ring (at least for the gaseous component). More interesting is the amount of structure present in the PVDs, especially in the inner parts of the model where the effects of the bar are strongest. We find back the signatures of the x_1 and x_2 orbits already discussed above, as well as the features which allow us to determine the viewing angle with respect to the major axis of the bar. The large gap between the signatures of the x_1 and outer 2:1 families of periodic orbits in the PVDs (partially filled in Fig. 3.8) is due to our reconstitution of the density distribution of a prototypical barred galaxy, which also has a gap between the distributions of the x_1 and outer 2:1 families. The only way to make this gap disappear is to populate periodic orbit families close to corotation, but this is not obvious using our periodic orbits approach. Beyond the 4:1 gap in the characteristic diagram, there are higher order n:1 families,

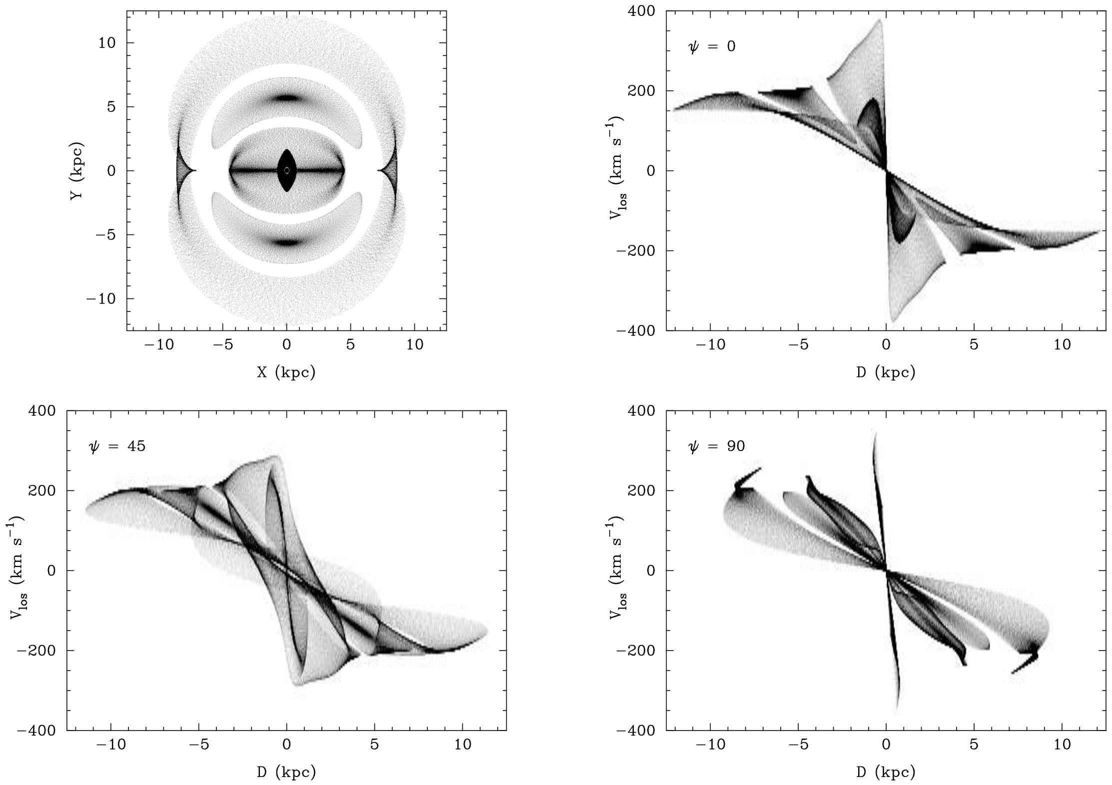

Figure 3.8: Same as Figure 3.4 but for the x_1, x_2, LPO, and outer 2:1 families of periodic orbits in model 001. Note that fewer viewing angles are displayed.

and, between consecutive 2n:1 gaps, short segments of what can still be called x_1 orbits (see Fig. 3.1 and Fig. 2 in A92a). However, as can be seen from the figures of A92b, the gas streamlines continue to be ellipsoidal and elongated along the bar past the IUHR, the extent of this region being very model dependent. Loosely speaking, one could say that, although the gas does not follow precisely the higher order resonance families, it follows their general form. Yet, further out the gas circulates around each of the two stable Lagrange points L_4 and L_5, the streamlines now being associated with the LPO periodic orbits (see Fig. 11 in Sellwood & Wilkinson 1993). The latter are easy to add in our description and have been included in Figure 3.8. Their signature in the PVDs is very similar to that of circular orbits. As expected, because of their location, the signature of the LPO orbits partially fills the gap between the signature of the x_1 orbits and that of the outer 2:1 orbits. The gap is significantly reduced, but many smaller gaps are still present, due to the non-homogeneous distribution of the orbits of the various families. Such gaps could not occur in an axisymmetric spiral galaxy.

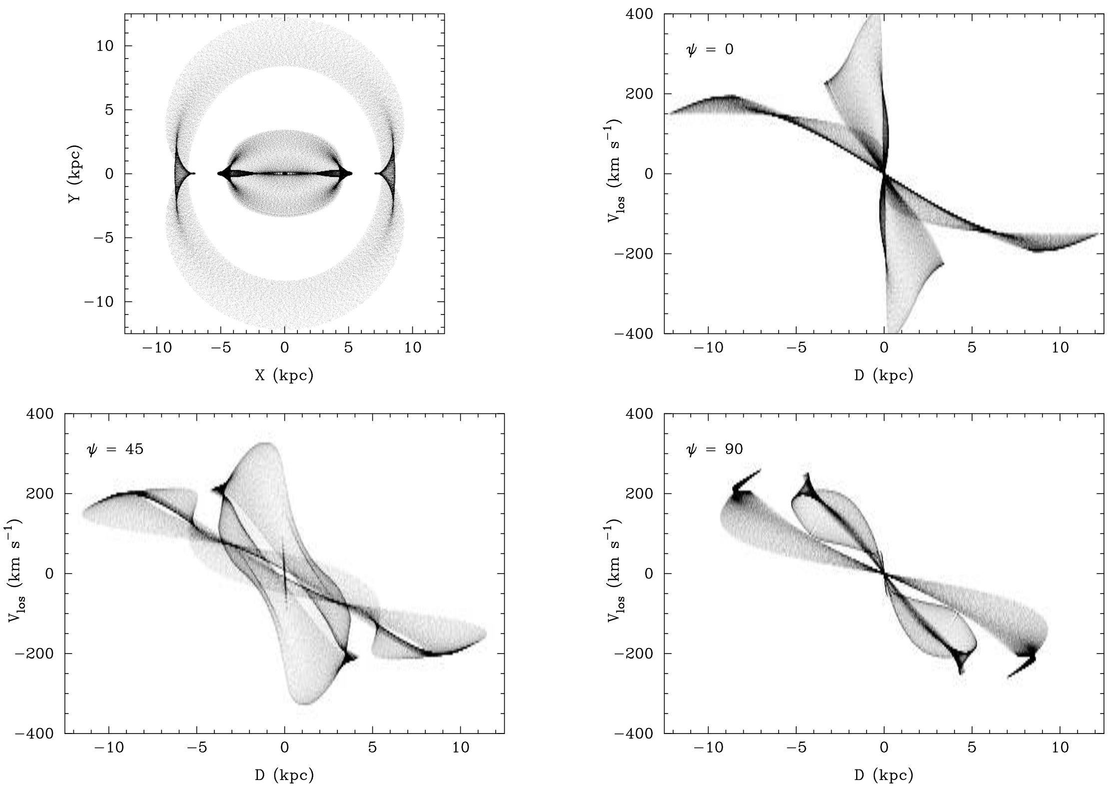

Figure 3.9: Same as Figure 3.4 but for the x_1 and outer 2:1 families of periodic orbits in model 086. Note that fewer viewing angles are displayed.

3.4.3 Model 086 (no-ILRs)

Despite the presence of ILRs in the classical sense (see Fig. 3.3), we consider model 086 a "no-ILRs" model because it does not have an x_2 family of periodic orbits. Its characteristic diagram is very similar to that of model 001 (see Fig. 3.1), differing only in the inner parts, where the x_2 and x_3 families are absent and the x_1 characteristic curve displays an elbow due to the high axial ratio of the bar (see also Fig. 4 of A92a; Pfenniger 1984). In addition, the x_1 orbits possess loops for a certain range of radii. Here, we exceptionally include those orbits to prevent the appearance of an empty region in the x_1 orbits surface density distribution.

Figure 3.9 shows the surface density and PVDs obtained by superposing the x_1 and outer 2:1 families of periodic orbits in model 086. The surface density distribution is again similar to that observed for the gaseous component of barred spiral galaxies. In the PVDs, as expected, the signature of the outer parts of the model has not changed compared to model 001, the outer 2:1 family of periodic orbits behaving again like a slowly-rising solid-body component (see Fig. 3.6). In the inner parts, the obvious difference with the PVDs of model 001 (Fig. 3.8) is the absence of any x_2 orbit signature (the LPO orbits have been omitted in Fig. 3.9 for clarity). On a qualitative level, the signature of the x_1 orbits has changed only slightly, the envelope still being generally parallelogram-shaped. The main difference with the signature of the x_1 orbits in model 001 is that the envelope of the signature has more curved edges, due to the presence of orbits with loops, and it reaches more extreme radial velocities (compared to the circular velocity), due to the higher axial ratio of the bar yielding more eccentric orbits (see Fig. 10 in A92a). The gap between the signatures of the x_1 and outer 2:1 orbits is again due to the absence of populated orbits near corotation in our model.

3.4.4 Other Models

Now that we understand the general structure of the PVDs produced by models with and without ILRs, we can extend our study to investigate how the bar diagnostics might change when the free parameters of the mass model are varied. To do this, we borrow heavily on the results of A92a, who studied how the orbital structure of the mass model varies within most of the volume of parameter space likely to be occupied by real galaxies. We do not expect the outer parts of the models to vary significantly since the influence of the bar falls off rapidly with radius. The outer families of periodic orbits will always produce slowly-rising almost solid-body signatures in the PVDs. We will thus concentrate on understanding the behaviour of the periodic orbits in the inner parts of the models.

The parallelogram-shaped signatures of the x_1 and x_2 periodic orbits in the PVDs will be mainly affected by the eccentricity and extent of the orbits. The results of A92a concerning the eccentricity of the x_1 orbits can be summarised as follows (see Fig. 10 in A92a): as the axial ratio of the bar a/b is increased, the Lagrangian radius r_L increased, the central concentration ρ_c increased, and/or the quadrupole moment of the bar Q_m decreased, the eccentricity of the x_1 orbits is increased. The counterintuitive behaviour of the eccentricity of the x_1 orbits with Q_m stems from the fact that for Q_m to be increased, the bulge mass and therefore the central density of the model has to be decreased (the total mass within a given radius being fixed), leading to a decrease of the eccentricity of the orbits. The eccentricity of the x_2 orbits behaves in the same way as that of the x_1 orbits, except with respect to the axial ratio of the bar (again, see Fig. 10 in A92a). In that case, the x_2 orbits become less eccentric as the bar axial ratio is increased. Because higher eccentricity means more extreme radial velocities compared to the circular velocity in the PVDs (very high radial velocities when an orbit is seen end-on and very low velocities when an orbit is seen side-on), the envelopes of the signatures of the x_1 and x_2 orbits in the PVDs should be most extreme (in the above sense) for high bar axial ratios (except for the x_2 orbits), high Lagrangian radii, high central densities, and/or low bar quadrupole moments. This was certainly the case for model 086, which has a higher bar axial ratio than model 001 (see Fig.3.4 and 3.9).

A92a showed that the radial extent of the x_1 family of periodic orbits is mainly affected by the pattern speed of the bar and changes very little as the other parameters of the mass model are varied (see Fig. 6 and 7 of A92a). For the x_2 orbits, the major factor affecting their signature in the PVDs will be their existence or non-existence, depending on the model considered. A92a showed that the radial range of the x_2 orbits is reduced when the bar axial ratio a/b and/or bar quadrupole moment Q_m are increased, and when the central density ρ_c and/or Lagrangian radius r_L are decreased (again, see Fig. 6 and 7 of A92a). Furthermore, as exemplified by model 086, the x_2 orbits can be completely absent for high bar axial ratios and/or bar quadrupole moments, and for low central densities and/or Lagrangian radii. The presence and extent of the inverted S-shape signature of the x_2 orbits in the PVDs depends therefore strongly on the parameters of the mass model.

Full sequences of PVDs as each parameter of the mass model is varied will be provided in Chapter 4, using hydrodynamical simulations. We do not present them here using the periodic orbits approach to avoid unnecessary repetition.

3.5 Discussion

The bar diagnostics we have developed in the previous sections are all based on the use of periodic orbit families in the equatorial plane of a barred spiral galaxy mass model. Periodic orbits, however, are only an approximation to the dynamical structure of either the gas or the stars in galaxies and the PVDs presented in the previous sections should only be used as a *guide* when interpreting kinematical data.

The ability of the gaseous component to dissipate energy changes its behaviour from that predicted by the periodic orbits, particularly near shocks, which occur at the transition regions between different orbit families and near periodic orbits with loops. The kinematics of the stars on regular orbits are relatively well approximated by that of the periodic orbits, since the former are trapped around the latter. On the other hand, stars on chaotic orbits give a totally different signature in the PVDs, and the percentage of stars on such orbits may well be non-negligible, particularly in strongly barred galaxies. In addition, when populating the periodic orbit families, we have not attempted to make the models self-consistent. We have only calculated the shape of the signature in the PVDs of each family of periodic orbits of the models, but not the relative weights of the families or the relative weights of the orbits within them. Nevertheless, in order to assess how much our results depend on the method adopted to populate the orbits, we have also produced PVDs for the x_1 and x_2 periodic orbits of model 001 using equal increments of the Jacobi energy between orbits (rather than equal Δy). As expected, the envelope of the signature of the x_1 orbits in the PVDs does not change, but, because of the form of the x_1 characteristic curve (see Fig. 3.1), the central parts are much stronger. Similarly, the signature of the x_2 orbits changes very little.

Independent of those issues, the relative amplitudes of the components of the PVDs will also vary depending on the emission line observed, this simply because the components arise from different parts of the galaxy, where the line might be produced in different ways. For example, increased star formation and/or shocks in some components will lead to different emission line strengths in those components, and the ratios between the components will depend on the line used to measure the kinematics.

When interpreting data based on the PVDs produced here, one should therefore take into account the following effects: 1) the kinematical signature observed might be somewhat different from that calculated here because periodic orbits are only an approximation to the gaseous or stellar dynamics of a galaxy, 2) the relative amplitudes of the components will be different from those calculated here because the building blocks approach used may not represent the relative weights correctly, and 3) the relative amplitudes of the components will be different from those calculated here because the intensity of a line depends not only on the density of the emitting material but also on the production mechanism of the line, which is not considered here. The hydrodynamical simulations reported in Chapter 4 address the first of those problems, although the gas is still not treated self-consistently. Being self-consistent, the N-body simulations reported in Paper III cover both the first and second problems (for stellar systems). However, to remedy the third problem raised above, one would need to consider both stellar evolution and the detailed physical conditions in the gas.

Another effect which might hinder our ability to detect bars in edge-on spiral galaxies is the presence of dust. Because dust in spiral galaxies is mostly confined to a thin layer, it can make disks optically thick at optical wavelengths if they are viewed edge-on. If this is the case, there are two ways around the opacity problem. Firstly, it is possible to select objects which are not perfectly edge-on. The line-of-sight then reaches the central parts of the galaxy, where the bar resides, while still going through a substantial fraction of the disk. However, if the inclination is too large, the bar diagnostics developed here will not work, as they depend on the line-of-sight going through most of the disk. Secondly, it is possible to use observations in a part of the spectrum where even a dusty disk is likely to be optically thin. Long-slit spectroscopy in the near-infrared (e.g. using the Brγ line at K-band) is attractive, but most lines are weak in non-active galaxies and near-infrared spectrographs with sufficient resolution for kinematical work are still uncommon. A better option is to use H I line-imaging with a radio synthesis telescope. Even very dusty edge-on spiral galaxies are probably optically thin at 21 cm. In addition, it is possible to use a higher spectral resolution than available with most optical long-slit spectrographs. However, because of limited sensitivity and spatial resolution, radio synthesis observations are useful only for large H I-rich galaxies. Using a large sample of galaxies, we will address in more detail in Chapter 5 the question of dust extinction when identifying bars in edge-on spiral galaxies.

3.6 Summary and Conclusions

Our main goal in this chapter was to develop kinematical bar diagnostics for edge-on spiral galaxies. Considering a well-studied mass model including a Ferrers bar, we identified the major periodic orbit families and briefly reviewed the orbital structure in the equatorial plane of barred spiral galaxies. We considered only orbits which are direct, singly-periodic, and non-self-intersecting. Using a simple method to populate the orbits, we then used the families of periodic orbits as building blocks to model the structure of real galaxies.

We constructed position-velocity diagrams (PVDs) of the models using an edge-on projection and various viewing angles with respect to the bar. We considered mainly two models which are prototypes of models with and without inner Lindblad resonances. The PVDs obtained show a complex structure which would not occur in an axisymmetric galaxy (see Fig. 3.8 and 3.9). The *global* appearance of the PVDs can therefore be used as a reliable bar diagnostic in edge-on disks. Specifically, the presence of gaps between the signatures of the various periodic orbit families in the PVDs follows directly from the non-homogeneous distribution of the orbits in a barred galaxy. The x_1 orbits lead to a parallelogram-shaped feature in the PVDs which reaches very high radial velocities with respect to the outer parts of the model when the bar is seen end-on and rather low velocities when the bar is seen side-on. This feature occupies all four quadrants of the PVDs, i.e. including the two forbidden quadrants. This signature would dominate the structure of the PVD produced by the stellar component of a barred spiral galaxy, and can be used as an indicator of the viewing angle with respect to the bar in an edge-on disk. When present, x_2 orbits can also be used reliably as a bar diagnostic and behave similarly to the x_1 orbits in the PVDs. However, the highest velocities are now reached when the bar is seen side-on and the signature is spatially much more compact. The signature of the x_2 orbits would dominate the structure of the PVD produced by the gaseous component of a barred spiral galaxy.

The mass model we adopted had four free parameters, allowing to reproduce the range of properties observed in real galaxies. Using the results of A92a, we analysed how the structures present in the PVDs vary when the parameters of the mass model are changed. We predicted that the signatures of the x_1 and x_2 periodic orbits should be more extreme for high bar axial ratios (except for the x_2 orbits), high Lagrangian radii, high central densities, and/or for low bar quadrupole moments. In addition, the extent of the x_2 family is reduced and the orbits can completely disappear when the bar axial ratio and/or bar quadrupole moment are increased and when the Lagrangian radius and/or central density are decreased. The shape and presence of the signatures of the x_1 and x_2 families of periodic orbits in a PVD can therefore provide strong constraints on the mass distribution of an observed galaxy.

We briefly discussed the application of the models to the interpretation of real data. The major limitations of the models are the approximation of the disk kinematics by that of periodic orbits, the treatment of the orbits as "test particles", and the ignorance of the production mechanism of the line observed. The understanding of the traces of individual periodic orbits in the PVDs, and of the signatures of the periodic orbit families, will prove very useful in Chapter 4 and in Paper III. In those, using hydrodynamical and N-body simulations, we will develop bar diagnostics similar to the ones discussed here and addressing some of the above limitations.

References

Athanassoula, E. 1992a, MNRAS, 259, 328 (A92a)

———. 1992b, MNRAS, 259, 345 (A92b)

———. 1996, in Spiral Galaxies in the Near-IR, ed. D. Minniti, and H.-W. Rix (Springer: Berlin), 147

Athanassoula, E., Bienayme, O., Martinet, L., & Pfenniger, D. 1983, A&A, 127, 349

Athanassoula, E., & Bureau, M. 1999, in preparation. (Paper III)

Athanassoula, E., Morin, S., Wozniak, H., Puy, D., Pierce, M. J., Lombard, J., & Bosma, A. 1990, MNRAS, 245, 130

Beaulieu, S. F. 1996, Ph. D. Thesis, The Australian National University

Binney, J., Gerhard, O. E., Stark, A. A., Bally, J., & Uchida K. I. 1991, MNRAS, 252, 210

Blitz, L., & Spergel, D. N. 1991, ApJ, 379, 631

Burstein, D. 1979a, ApJS, 41, 435

———. 1979b, ApJ, 234, 829

Buta, R. 1986, ApJS, 61, 609

Buta, R., & Crocker, D. A. 1991, AJ, 102, 1715

Combes, F., Debbasch, F., Friedli, D., & Pfenniger, D. 1990, A&A, 233, 82

Combes, F., & Sanders, R. H. 1981, A&A, 96, 164

Contopoulos, G. 1980, A&A, 81, 198

———. 1988, A&A, 201, 44

Contopoulos, G., & Grosbøl, P. 1989, A&A Rev., 1, 261

Contopoulos, G., & Papayannopoulos, T. 1980, A&A, 92, 33

de Carvalho, R. R., & da Costa, L. N. 1987, A&A, 171, 66

Ferrers, N. M. 1877, Q.J. Pure Appl. Math., 14, 1

Fux, R. 1997, A&A, 327, 983

———. 1997, Ph. D. Thesis, Université de Genève

Hamabe, M., & Wakamatsu, K. 1989, ApJ, 339, 783

Kalnajs, A. J. 1973, PASA, 2, 174

Kuijken, K., & Merrifield, M. R. 1995, ApJ, 443, L13

Kuzmin, G. 1956, AZh, 33, 27

Merrifield, M. R. 1996, in Barred Galaxies, ed. R. Buta, D. A. Crocker, and B. G. Elmegreen (ASP: San Francisco), 179

Mulder, W. A., & Liem, B. T. 1986, A&A, 157, 148

Papayannopoulos, T., & Petrou, M. 1983, A&A, 119, 21

Peters, W. L. 1975, ApJ, 195, 617

Pfenniger, D. 1984, A&A, 134, 373

Press, W. H., Flannery, B. P., Teukolsky, S. A., & Vetterling, W. T. 1986, Numerical Recipes (Cambridge: Cambridge University Press)

Raha, N., Sellwood, J. A., James, R. A., & Kahn, F. D. 1991, Nature, 352, 411

Sandage, A. 1961, The Hubble Atlas of Galaxies (Washington: Carnegie Institution)

Sanders, R. H., Teuben, P. J., & van Albada, G. D. 1983, in Internal Kinematics and Dynamics of Galaxies, ed. E. Athanassoula (Reidel: Dordrecht), 221

Sanders, R. H., & Tubbs, A. D. 1980, ApJ, 235, 803

Schwarz, M. P. 1985, MNRAS, 212, 677

Schwarzschild, M. 1979, ApJ, 232, 236

Sellwood, J. A., & Wilkinson, A. 1993, Re. Prog. Phys., 56, 173

Sevenster, M. S., Saha, P., Valls-Gabaud, D., & Fux, R. 1997, MNRAS, submitted.

Sparke, L. S., & Sellwood, J. A. 1987, MNRAS, 225, 653

Teuben, P., & Sanders, R. H. 1985, MNRAS, 201, 303

Toomre, A. 1963, ApJ, 138, 385

Tsikoudi, V. 1980, ApJS, 43, 365

van Albada, T. S., & Sanders, R. H. 1982, MNRAS, 201, 303

Wada, K., Taniguchi, Y., Habe, A., & Hasegawa, T. 1994, ApJ, 437, L123

Wakamatsu, K., & Hamabe, M. 1984, ApJS, 56, 283

Weiland, J. L., et al. 1994, ApJ, 425, L81

Weiner, B. J., & Sellwood, J. A. 1995, BAAS, 186, 884

Wozniak, H. 1994, A&A, 286, L5